

# Fast optical variability in supergiant X-ray binaries

D. Di Filippantonio<sup>1</sup>, P. Reig<sup>2,3</sup>, and J. Fabregat<sup>4</sup>

<sup>1</sup> Universidad Internacional de Valencia, Calle Pintor Sorolla, 21, 46002, Valencia, España  
e-mail: denis.df@gmail.com

<sup>2</sup> Institute of Astrophysics, Foundation for Research and Technology, 71110 Heraklion, Crete, Greece  
e-mail: pau@physics.uoc.gr

<sup>3</sup> University of Crete, Physics Department & Institute of Theoretical & Computational Physics, 70013 Heraklion, Crete, Greece

<sup>4</sup> Observatorio Astronómico de la Universidad de Valencia, Calle Catedrático José Beltrán 2, 46980 Paterna, Valencia, Spain  
e-mail: juan.fabregat@uv.es

Received ; accepted

## ABSTRACT

**Context.** Recent studies of massive stars using high-precision space photometry have revealed that they commonly exhibit stochastic low-frequency variability.

**Aims.** The main goal of this work is to investigate the fast photometric variability of the optical counterparts to supergiant X-ray binaries and to compare the general patterns of this variability with that observed in the Galactic population of other early-type stars.

**Methods.** We selected a sample of 14 high-mass X-ray binaries with supergiant companions observed by the Transiting Exoplanet Survey Satellite (TESS). We also studied 4 Be/X-ray binaries with persistent X-ray emission for comparison. The TESS light curves were created from the full-frame images using the `Lightkurve` package. The light curves were background subtracted and corrected for scattered light and instrumental effects. Standard Fourier analysis was used to obtain the periodograms. We used a phenomenological model to fit the amplitude spectra and derive the best-fit parameters.

**Results.** All sources exhibit fast aperiodic light variations. The shape of the periodogram is well described by a red noise component at intermediate frequencies ( $\sim 1 - 10 \text{ d}^{-1}$ ). At lower frequencies, the noise level flattens, while at higher frequencies the periodogram is dominated by white noise. We find that the patterns of variability of the massive companions in supergiant X-ray binaries agree with those of single early-type evolved stars in terms of the general shape of the periodograms. However, they exhibit higher amplitude at low frequencies and lower characteristic frequencies than those of Be/X-ray binaries. Unlike Be/X-ray binaries, supergiant X-ray binaries exhibit a total lack of coherent signals at high frequencies. Most sources have been analyzed over multiple TESS sectors, spanning a duration of 4 years. We do not find any significant variation over time in the low-frequency variability characteristics.

**Conclusions.** This study reveals that stochastic low-frequency variability is a very common, if not ubiquitous, feature intrinsic to supergiant optical companions in X-ray binaries. The phenomenology of this variability is similar to that of single early-type supergiant stars.

**Key words.** Stars: supergiants – Stars: early-type – Stars: oscillations – X-rays: binaries – Stars: neutron

## 1. Introduction

High-mass X-ray binaries (HMXBs) are divided into supergiant X-ray binaries (SGXBs) and Be/X-ray binaries (BeXBs) according to the luminosity of the optical counterpart. In a SGXB (Martínez-Núñez et al. 2017; Kretschmar et al. 2021), a neutron star orbits around an evolved star (luminosity class I or II), while in BeXBs (Reig 2011; Paul & Naik 2011) the optical companion is a main sequence star (luminosity class III–V). In Be stars, episodic ejection of mass from their atmospheres results in the formation of a flattened disk around their equator (Porter & Rivinius 2003; Rivinius et al. 2013). Rotation and pulsations are characteristics of the fast optical variability in BeXBs and manifest as multifrequency photometric variability (Baade et al. 2016; Rivinius et al. 2016; Semaan et al. 2018; Balona & Ouzar 2020, 2021) and as spectroscopic variability, for example in the form of line-profile variations (Baade 1984; Rivinius et al. 1998, 2003; Balona 2003; Zima 2006) with typical periods in the range of 0.1 to 2 days. In SGXBs, the supergiant star produces powerful stellar winds that supply the material accreted onto the compact object. Most known SGXB systems transfer mass from the donor to the neutron star via this mechanism. However, in

a handful of systems, the mass transfer occurs most likely via Roche lobe overflow (RLOF), which leads to a higher mass flow. In such cases, an accretion disk is formed around the neutron star and the X-ray emission is increased (Corbet 1986; Kretschmar et al. 2019).

A subclass of SGXBs are the supergiant fast X-ray transients (SFXT), which are similar to the other SGXBs in the sense that they contain an OB supergiant as the mass donor and that the mass-transfer mechanism is through stellar wind. The difference lies in the fact that, while other SGXB systems show a relatively constant emission in the X-ray range, the SFXTs present transient X-ray emission with fast outbursts, corresponding to a variable amount of material being transferred from the supergiant to the compact object (Negueruela et al. 2006; Kretschmar et al. 2019).

The advent of space-based high-accuracy photometry missions, such as *Kepler* (Koch et al. 2010) and TESS (Ricker et al. 2015), has enabled detailed studies of the short-term variation of stellar luminosity, which, through asteroseismology, allows us to probe the internal structure of the star. In particular, the detection and analysis of the coherent pulsation modes and stochastic low-frequency (SLF) variability of massive stars

have only recently been made possible through this new set of long-duration, high-accuracy photometry measurements (Aerts et al. 2017; Tkachenko et al. 2014; Bowman et al. 2019b; Dorn-Wallenstein et al. 2019; Bowman et al. 2020; Dorn-Wallenstein et al. 2020).

In Reig & Fabregat (2022), we studied the fast optical variability of BeXBs. The motivation behind that study was to investigate if the same phenomenology is observed in the short-term variability of Be stars regardless of whether they belong to an X-ray binary or are single systems. In other words, our aim was to find out whether or not the neutron star affects the rapid optical variability properties. We found that BeXBs and classical Be stars are indistinguishable in terms of their pulsational characteristics.

SGXBs have shorter orbital periods than BeXBs, and therefore the neutron star passes closer to the optical companion (Kim et al. 2023). In a similar approach to that applied to BeXBs, in the present work we intend to compare the rapid optical variability of massive companions in X-ray binary systems with that of single supergiant stars. Likewise, we compare the variability properties of SGXBs with persistent (in X-rays) BeXBs. The X-ray luminosity of persistent BeXBs is two or three orders of magnitude lower than of transient BeXBs during outbursts, indicating that they accrete from the stellar wind of the companion and/or from the outer parts of a highly debilitated disk and are not expected to show a strong neutron-star–disk interaction. Persistent BeXBs exhibit more stable mass loss, and display optical light curves similar to those of SGXBs in terms of their variability properties (Reig & Roche 1999).

Unlike Be stars, whose amplitude spectra are dominated by coherent pulsation modes attributed to non-radial pulsations caused by changes in the opacity and opacity gradient in different stellar layers (Pamyatnykh 1999, see also Aerts 2021 for a review), SLF variability in massive evolved stars is caused by some kind of turbulence or instability within the star, such as waves excited from near the convective core and/or near the surface (see Bowman 2023, for a recent review). This work focuses on the analysis of SLF variability in SGXB systems, and their comparison to BeXBs and isolated supergiants.

## 2. Observations

We used data assembled by the Transiting Exoplanet Survey Satellite (TESS). The primary objective of TESS is to discover new exoplanets using the transit method and the instrument is optimized for the detection of super-Earth-sized planets around nearby bright stars (Ricker et al. 2015). However, owing to its observational strategy, TESS covers the entire sky in periods of two years. This makes TESS an excellent mission for monitoring the variability of many different types of objects. In particular, TESS has opened up the sky for massive studies of stellar variability (e.g., Burssens et al. 2020), where previous missions focused generally on low-mass stars.

The TESS instrument is comprised of four cameras with a wide field of view of  $24^\circ$  by  $24^\circ$ , which means a strip of  $24^\circ$  by  $96^\circ$  is observed at any given time. The cameras and CCD detectors are optimized for the red band, and are sensitive in the 600 to 1000 nm range, as the primary mission objective is to survey stars with spectral types from F5 to M5. Each camera is composed of 4 CCDs of 2048x2048 pixels, corresponding to a relatively low spatial resolution of 21 arcsec per pixel.

The CCDs are read out at two-second intervals and are then stacked on board to produce lower-frequency data to be down-linked to Earth. Small windows around a predefined list of tar-

gets of interest (TOIs) are stacked over a duration of 2 minutes, while the complete CCD readout in the form of full-frame images (FFIs) are stacked over a longer duration. During the primary mission (July 2018 to July 2020, sectors 1 to 26), the FFIs were sampled with a cadence of 30 minutes; during the first mission extension (July 2020 to August 2022, sectors 27 to 55), this cadence was 10 minutes; and for the second mission extension (since September 2022, sector 56), this cadence was 200 seconds. The spacecraft observes the same direction of the sky for two orbits, or 27.4 days, with this being referred to as one sector, before moving to a new observation region.

## 3. Methodology

This section describes the overall methodology and the various steps followed from obtaining the TESS science data to computing the best-fit model parameters.

### 3.1. Selection of sources

To compile the list of HMXBs to be analyzed, we referred to consolidated catalogs of HMXBs (Kim et al. 2023; Fortin et al. 2023; Neumann et al. 2023). In particular, Fortin et al. (2023) produced a catalog of galactic HMXBs with confirmed optical counterparts, which also includes a classification by HMXB type, simplifying the selection of objects. As the focus of the present project is on SGXBs, the list of objects was initially filtered to only include objects whose optical companion is a supergiant star. This selection resulted in a total of 54 objects.

The next step was to check if these sources had a clear optical counterpart bright enough to extract a light curve using TESS FFI data, and far enough from any bright source so as to be separated in the TESS data, which have a limited spatial resolution (21 arcsec per pixel). Of the 54 preselected sources, 12 were not observed by TESS and another 20 were too faint to extract a useful light curve. Finally, 8 objects were eliminated due to their proximity ( $< 2$  pixels) to another object as bright or brighter ( $> 1$  mag), which prevented us from extracting a clean light curve.

A total of 14 SGXBs remained in the list of objects to be analyzed, which included two peculiar systems with supergiant companions, even though they are not typical SGXBs. These are XTE J0421+560 with a B[e] supergiant and 4U 1954+319 with a later-type M supergiant star. Four persistent BeXB sources were added to the list in order to compare them with the results obtained for the SGXBs.

The final list of objects is shown in Table 1, where the sources are sorted first by type and then by right ascension (RA). For each object, the list of sectors that contain valid data is provided. This amounts to a total of 70 sectors for all sources combined.

### 3.2. Data processing

We created our own light curves from the FFIs using the LIGHTKURVE (Lightkurve Collaboration et al. 2018) and TESScut (Brasseur et al. 2019) packages to download a target pixel file (TPF) with an  $N \times N$  pixel image centered on the target for every available TESS sector. The size of the cutout is important for the processing of the light curve in the subsequent steps. In particular, it should be large enough to include enough background pixels to correct the raw light curve for scattered light—in addition to the aperture mask discussed in the following section. However, it should also be kept in mind that larger cut-

**Table 1.** Selected list of sources

Object	Type	Sp.Typ.	G (mag)	$P_{orb}$ [d]	$P_{spin}$ [s]	Mass ( $M_{\odot}$ )	TESS ID	TESS sectors
IGR J00370+6122	SGXB	BN0.7Ib	9.5	15.665	674	22	284207391	17,18,24,58
2S 0114+650	SGXB	B1Iae	10.5	11.598	10008	16	54469882	18,24,25,52,58
Vela X-1	SGXB	B0.5Iae	6.7	8.963	283	26	191450569	08,09,35,62
Cen X-3	SGXB	O6-7II-III	12.9	2.033	4.802	20.2	468240308	10,11,37,64
1E 1145.1-6141	SGXB	B2Iae	12.3	14.365	298	14	324122933	10,11,37,38,64
4U 1538-522	SGXB	B0.2Ia	13.2	3.728	526.4	20	190415214	12,39,65
4U 1700-377	SGXB	O6Ia	6.4	3.412	–	46	347468930	12,39,66
Cyg X-1	SGXB	O9.7Iab	8.5	5.599	–	40.6	102604645	14,54,55,74,75
IGR J08408-4503	SFXT	O8.5Ib-II	7.5	9.54	–	33	141856104	08,09,35,61,62
IGR J11215-5952	SFXT	B1Ia	9.8	164.6	186.8	–	451004619	10,11,37,64
IGR J16465-4507	SFXT	B0.5-1Ib	13.5	30.24	228	27.8	236510713	12,39,66
XTE J1739-302	SFXT	O8Iab	12.6	51.47	–	33.7	106579192	39
RX J0146.9+6121	BeXB	B1IIIe	11.2	330	1407.4	9.6	399437313	58
X Per	BeXB	B1Ve	6.3	250.3	837.7	15.5	94471007	18,43,44,70,71
4U 1036-56	BeXB	B0III-Ve	11.2	60.9	860	17.5	458199429	10,36,37,63,64
4U 2206+543	BeXB	O9.5Ve	9.7	9.558	392	18	328546890	16,17,56,57
XTE J0421+560	sgB[e]	B0/2I[e]	10.8	19.41	–	–	418090700	19,59,73
4U 1954+319	sg(M)	MI	8.4	1296.6	18612	9	87456211	14,41,54,55,74,75

**Notes.** Periods and mass from Fortin et al. (2023)

outs will lead to excessive amounts of data to download and process without any advantage to the final light curve. After several iterations with various objects, a cutout size of 15 by 15 pixels ( $5.25 \times 5.25 \text{ arcmin}^2$ ) was found to be adequate and was used for all sources.

The raw light curve was computed from the TPF by summing the flux over a defined aperture mask for each cadence, and obtaining a total flux over time for the whole duration of the sector. For each object, it is therefore necessary to define an aperture mask that best covers the target object without including bright contaminating sources.

A source mask was defined from pixels in the TPF, which show a median flux that is brighter than the threshold multiplied by the standard deviation above the overall median. Generally, we used a threshold of  $S/N=15$  for brighter sources ( $G < 10$ ) but this was decreased to  $S/N = 5$  for fainter sources. Custom-made masks were defined for 1E 1145.1-6141, Cen X-3, IGR J16465-4507, XTE J1739-302, and Cyg X-1 to avoid including light from nearby stars. The background mask was defined avoiding field sources (i.e. pixels with fluxes below the null threshold).

The light curves were also corrected for scattered light using the regression corrector method<sup>1</sup>. Finally, because the goal of this project is not to analyse long-term variations of the sources but to study the SLF variability, long-term trends were removed from the light curves when present. None of the SGXB, SFXT, or wind-fed BeXB sources (4U 2206+543 and 4U 1026-56) showed any noticeable long-term variability on the sectors observed. In contrast, the BeXB sources X Per and RX J0146.9+6121 show long-term variability in all the analyzed sectors. Long-term variability is a common behavior of Be stars, with slow quasi-periodic variation over periods of month to years (Reig & Fabregat 2022).

### 3.3. Extraction of significant frequencies and pre-whitening

Significant coherent signals are not expected in luminous SGXBs (type Ia), although they may be present in less luminous

systems (type Ib or II). Bowman et al. (2019b) assembled a sample of 167 hot massive stars (91 supergiants and 76 stars with luminosity class III-V or unknown luminosity) with the purpose of investigating the incidence of coherent modes and stochastic variability. Only two supergiant systems showed  $\beta$  Cephei-like pulsations, while all (except one) type Ia supergiants (29 systems) exhibited a frequency spectrum consistent with SLF variability without any other kind of coherent modulation. Only one system presented a modulation that could be attributed to rotation by a clumpy aspherical wind. In contrast, almost all BeXBs display multi-periodic light modulations attributed to non-radial pulsations (Reig & Fabregat 2022).

To remove the periodic component, we performed the following steps (a process known as pre-whitening; see e.g., Bowman & Michielsen 2021, and references therein):

1. Compute the periodogram.
2. Extract the frequency of the highest peak  $f_{max}$ .
3. Fit the time series with a function of the type

$$A \sin(2\pi f_{max} t + \phi).$$

4. Subtract the fitted curve from the time series to obtain the residuals.
5. Compute the periodogram of the residuals.
6. Compute the signal-to-noise ratio of the peak, where the signal is the amplitude  $A$  of the peak and the noise is the mean level of the surrounding continuum.
7. If the peak is significant ( $S/N > 4$ ), we annotate its frequency and amplitude and proceed again to step 1.

This iterative process allows us to detect all significant pulsations and obtain a pre-whitened light curve, which should only contain random noise components, or at least a combination of non-significant frequencies. We note that some authors (see e.g., Bowman & Michielsen 2021) have warned against the use of four times the noise level as the optimum criterion to extract significant frequencies, arguing that this is too low, and includes some fraction of peaks whose origin is simply white noise. Nevertheless, as we compare our work with previous works that used the same criterion, we opted to use  $S/N > 4$ .

<sup>1</sup> <https://heasarc.gsfc.nasa.gov/docs/tess/NoiseRemovalv2.html>

Another critical decision is the width of the frequency interval around the peak to compute the noise level. An overly broad interval would include mostly the white noise component at higher frequency, and all the apparent peaks at low frequency would appear to have  $S/N > 4$ , even though they are simply random variation around the mean periodogram level. On the other hand, an excessively narrow interval may include part of the signal as noise, especially when red noise is present, decreasing the significance of the peak. In this work, the noise level is computed using a moving median in log space with a filter width of equal to 0.2 in log 10 space.

### 3.4. Light-curve gaps and interpolation

The obtained light curves are sampled at a constant frequency that depends on the sector, but contain a variable amount of gaps. Some of the gaps are due to planned outage in the measurements and others are due to invalid data in the archive, such as those from excess scattered light. Because of the change in the TESS operational strategy, light curves from sectors up to 55 have a large gap in the middle of the sector of the order of 1 to 2 days. Subsequent sectors do not have such large gaps, but have three gaps of around 5.25 hours every 6.85 days, which is half the TESS orbital period. We performed a statistical study of the gaps present in our light curves, finding that 70 light curves processed have 230 gaps of more than 1 hour, 70 gaps of more than 6 hours, and 50 gaps of more than 1 day.

The periodograms are computed using the Lomb-Scargle method, which in principle is designed to handle gaps and unevenly sampled data in time series. However, we noticed that in four light curves for sectors above 55, the computed periodogram showed strong artefacts linked to the periodic data gaps, which were not representative of the real periodogram of the source. This artificial effect was eliminated by performing a linear interpolation of the light curve over these short gaps, which introduces only a minor modification to the light curve. For consistency, the same process was followed for the light curves of all the sources. We note that the filled gaps (less than 6 hours) are short compared to the characteristic timescales of the SLF variability being analyzed. In addition, only a few gaps per sector were filled, such that the total number of data points added by interpolation amounted to less than 4 percent of the overall dataset (i.e., less than 1 day over the 27 day sector). Larger gaps were left unmodified as interpolating them would have a greater affect on the frequency content of the time series.

### 3.5. Periodograms

After detrending and pre-whitening, the final light curves were obtained and a periodogram was computed for each sector. The pre-whitened light curves consist of stochastic signals and therefore their power spectrum is very noisy. A standard method to reduce the noise in the periodograms is to perform averaging in the frequency domain. In this method, the data are divided up into segments of equal duration, a power spectrum is obtained individually for each segment, and then the resulting power spectra are averaged. In this work, we average the periodograms obtained in each sector to obtain a single mean periodogram per source in addition to the individual periodograms per sector.

The time series are available at different sampling frequencies (see Sect. 2), and therefore the maximum frequency sampled in the periodograms (Nyquist frequency) is different for data obtained at different epochs. However, as the averaging

method requires all the periodograms to have the same frequency range and resolution, we limited the frequency range of all periodograms to the lowest Nyquist frequency, which is  $24 \text{ d}^{-1}$ . Before computing the periodogram, and to account for the different white noise level resulting from the different sampling frequency, the time series were re-sampled at a cadence of 30 minutes by averaging over three data points (sectors 27 to 55) or six data points (from sector 56).

While the  $24 \text{ d}^{-1}$  frequency range is sufficient to analyze the SLF variability, and even to extract higher-frequency peaks corresponding to coherent pulsations, in particular in BeXBs, this limited frequency range made the estimate of the white noise component less reliable, revealing significant variability between sectors. In any case, as the parameters of interest are the characteristics of the low-frequency noise component, this frequency range was deemed acceptable within the scope of this work. This aspect is discussed in more detail in Sect. 4.2.2.

### 3.6. Noise-model fitting

The present work focuses on the analysis of SLF variability in SGXB systems, and their comparison to BeXBs and isolated supergiants. The detection of low-frequency variability in a large sample of OB supergiant stars in Bowman et al. (2019b) demonstrates the ubiquity of such phenomena in these stars. This type of low-frequency variability has been described in the literature as “red noise”, a type of correlated signal whose amplitude decreases as a function of frequency. This red noise is not due to measurement errors but is instead an intrinsic stochastic source of variability in the observed object.

In the present work, we model the characterization of this variability in the frequency domain by fitting the amplitude spectrum  $\alpha(f)$  of the normalized light curves with the function

$$\alpha(f) = \frac{\alpha_0}{1 + \left(\frac{f}{f_c}\right)^\gamma} + \alpha_w, \quad (1)$$

where  $\alpha_0$  is the amplitude of the SLF variability at zero frequency,  $f_c$  is its characteristic frequency, and  $\gamma$  is the roll-off slope in logarithmic scale. The term  $\alpha_w$  is used to model the white noise component of the spectrum, which is dominant at higher frequency. The characteristic frequency is the inverse of the characteristic timescale  $f_c = (2\pi\tau)^{-1}$ , where  $\tau$  can be understood as the duration of the dominant structures in the light curve (Stanishev et al. 2002; Blomme et al. 2011).

This model has been used by many authors to characterize this type of variability in various types of stars, for example for early-type stars in Bowman et al. (2019b,a, 2020), for yellow/red supergiants in Dorn-Wallenstein et al. (2020), for Wolf-Rayet stars in Lenoir-Craig et al. (2022), and for luminous blue variables in Dorn-Wallenstein et al. (2019) and Nazé et al. (2021)

To fit this model to the periodogram, we employed the routine `curve_fit` of `SciPy`, which uses non-linear least squares to fit a given function to input data by minimizing either the sum of the square of the residuals or, if a standard deviation is provided for each data point, the  $\chi^2$  value. Following Bowman et al. (2019a) and Dorn-Wallenstein et al. (2019), we performed the fit on the logarithm of the amplitude spectrum instead of performing it on the amplitude spectrum itself, as it is less sensitive to individual peaks in the periodogram.

To estimate the quality of the best-fit model, two indicators were computed: the reduced chi squared  $\chi_{\text{red}}^2$  and the probability  $Q$ . A value of  $\chi_{\text{red}}^2$  of close to unity indicates a good model

**Table 2.** Main frequencies detected.

Object	Type	Sp.Typ.	Main frequencies
IGR J00370+6122	SGXB	BN0.7Ib	none significant
2S 0114+650	SGXB	B1Iae	none significant
Vela X-1	SGXB	B0.5Iae	weak peak at 0.22 d <sup>-1</sup> (S/N: 5)
Cen X-3	SGXB	O6-7II-III	strong peak at 0.96 d <sup>-1</sup> (S/N: 26 - 38)
1E 1145.1-6141	SGXB	B2Iae	none significant
4U 1538-522	SGXB	B0.2Ia	peak at 0.535 d <sup>-1</sup> (S/N: 10)
4U 1700-377	SGXB	O6Ia	peak at 0.586 d <sup>-1</sup> (S/N: 6 - 10)
Cyg X-1	SGXB	O9.7Iab	weak peak at 0.36 d <sup>-1</sup> (S/N: 5 - 9)
IGR J08408-4503	SFXT	O8.5Ib-II	weak peak at 0.27 d <sup>-1</sup> (S/N: 5 - 8)
IGR J11215-5952	SFXT	B1Ia	none significant
IGR J16465-4507	SFXT	B0.5-IIb	very strong peak at 7.37 d <sup>-1</sup> + harmonics
XTE J1739-302	SFXT	O8Iab	none significant
RX J0146.9+6121	BeXB	B1IIIe	frequency groups around 1.5 and 2.9 d <sup>-1</sup>
X Per	BeXB	B1Ve	various groups around 1.2, 1.7, 2.88 and 3.6 d <sup>-1</sup>
4U 1036-56	BeXB	B0III-Ve	weak peak at 4.9 d <sup>-1</sup> (S/N: 5)
4U 2206+543	BeXB	O9.5Ve	weak peak at 6.15 d <sup>-1</sup> (S/N: 6)
XTE J0421+560	sgB[e]	B0/2I[e]	strong peak at 2.46 d <sup>-1</sup> (S/N: 18-30)
4U 1954+319	sg(M)	MI	main peak at 4.2 d <sup>-1</sup> with variable amplitude

fit, where the data points are coherent with the model and the estimated error of the data. However, what can be considered “close” depends on the number of degrees of freedom of the fit. For this reason, the additional indicator  $Q$ , which gives the probability that the chi-square will exceed a particular value  $\chi^2$  by chance if the model is correct, allows us to estimate the goodness of fit. If  $Q$  is a very small probability for some particular data set, then the apparent discrepancies are unlikely to be chance fluctuations. In general, a value of  $Q$  above 0.001 is acceptable (Press et al. 1993, chapter 15).

## 4. Results

In this section, we present the results of our analysis. More details on individual sources can be found in the Zenodo repository at <https://zenodo.org/uploads/14328326>.

### 4.1. Significant frequencies

As explained in Sect. 3.3, prior to the computation of the periodogram, the light curves were searched for the presence of coherent signals. In general, the periodograms for all the analyzed SGXBs are featureless above 2 d<sup>-1</sup>, with no significant peaks at high frequency, but instead a progressive increase in the amplitude level towards low frequencies, in line with SLF variation in the form of a “red noise” on top of the white noise floor level, which dominates at higher frequencies.

Table 2 presents a summary of the presence or absence of significant frequencies for each object. The complete list of significant frequencies detected, along with their amplitude and S/N, is provided in Appendix A.

#### 4.1.1. SGXBs

Five of the SGXBs systems show a significant peak at low frequency, corresponding to twice the orbital frequency of the system. The most obvious example is Cen X-3, for which the light curves of the four sectors show a clear pattern of double-wave ellipsoidal light variation, with two equal maxima and two un-

equal minima per orbital period, which are produced by the revolution of a tidally deformed star along its orbit (van Paradijs et al. 1983). The peak in the periodogram is detected at 0.96 d<sup>-1</sup>, which is close to twice the orbital frequency given the orbital period of 2.03 days. Slow periodic variation can be seen in the light curves of 4U 1538-522 and 4U 1700-377 as well, but in this case the exact pattern of the variation is less obvious as it is mixed with a higher level of stochastic variability. In any case, the detected peaks in their periodograms at 0.535 d<sup>-1</sup> and 0.586 d<sup>-1</sup> are equal to twice the orbital frequency, given their respective orbital periods of 3.73 and 3.41 days, respectively. A similar observation can be made in the periodograms of Cyg X-1 and Vela X-1, although in these cases it is much harder to detect any clear periodic variation in the light curves due to the longer periods involved. It should be highlighted that the frequencies detected are identical in all the sectors of these sources.

The SFXT IGR J08408-4503 shows a low-amplitude peak at 0.27 d<sup>-1</sup>, which is also close to twice the orbital frequency, given the orbital period of 9.5 days. We note that this peak is relatively small and is only detected in three out of five sectors.

The only exception to this general behavior is seen in IGR J16465-4507, which is classified as an SFXT, and shows  $\beta$  Cephei-like pulsation with a high-frequency peak at 7.37 d<sup>-1</sup>, with an amplitude of around 8 ppt, and harmonics of 14.75 d<sup>-1</sup> and 22.12 d<sup>-1</sup>. This source is discussed in more detail in Sect 5.3.

Finally, the remaining SGXBs/SFXTs do not show a significant peak above the red noise level. We point out that these systems all have longer orbital periods, which would make detecting any existing peak more difficult, given the 27 day duration of the sectors.

#### 4.1.2. BeXBs

X Persei has a large number of significant frequencies in various groups, which vary over time. The presence of such frequency groups is characteristic of Be stars, although not all pulsating Be stars display them (e.g., Baade et al. 2018; Reig & Fabregat 2022). Sector 18 has mostly two groups, around 1.7 d<sup>-1</sup> and

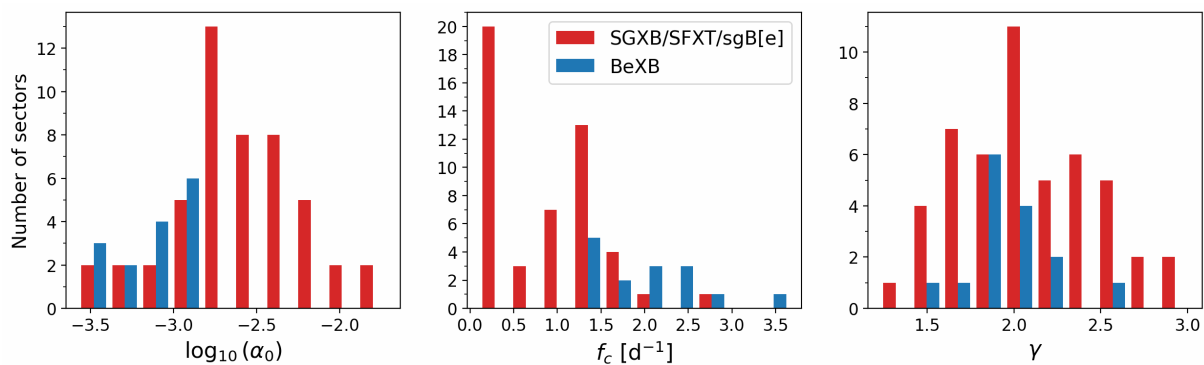


**Fig. 1.** SLF parameters: Histograms per sector and BeXB/SGXB.

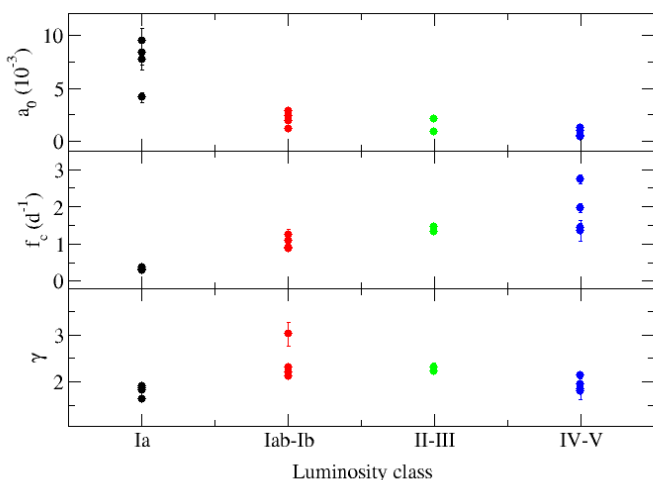


**Fig. 2.** Best-fit parameters of the SLF variability as a function of luminosity class.

$3.6 \text{ d}^{-1}$ , which also appear in sectors 43 and 44 in addition to an isolated peak at  $2.88 \text{ d}^{-1}$ . On the other hand, sectors 70 and 71 have a group around  $1.2 \text{ d}^{-1}$  and another around  $3.7 \text{ d}^{-1}$ . In addition, some sectors show peaks at higher frequency, but with lower amplitude.

RX J0146.9+6121 shows a fairly similar pattern to X Persei. In this case, the main groups are around  $1.5 \text{ d}^{-1}$  and  $2.9 \text{ d}^{-1}$  and it also has some other peaks at higher frequency with lower amplitude. This source was observed in only one sector, and so it is not possible to assess any variability over time.

In the case of 4U 1036-56 and 4U 2206+543, the periodograms are quite different as they do not contain a large number of significant frequencies, but instead are mostly dominated by a red noise component at low frequency and a lower white noise component, similar to what is seen in SGXBs. However, contrary to the SGXBs, there are some peaks at higher frequencies, which stand out above the noise level.

For 4U 2206+543, there is a peak at  $6.15 \text{ d}^{-1}$ , which is detected in all sectors, with a small amplitude of only 0.8 ppt. In the case of 4U 1036-56, a peak at  $4.9 \text{ d}^{-1}$  is detected in sectors 10, 36, and 37 with an amplitude of around 1 ppt and a peak at  $1.8 \text{ d}^{-1}$  is detected in sectors 10 and 37 with an amplitude of around 2 ppt. In sectors 63 and 64, these peaks are below  $S/N = 4$ .

#### 4.1.3. Other sources

The source XTE J0421+560 is the only one in the list classified as sgB[e]. This source shows some long-term variability, which is more in line with BeXB sources than SGXBs. In terms of the periodograms, XTE J0421+560 shows a strong peak at  $2.46 \text{ d}^{-1}$  for all three sectors, and another peak at  $1.09 \text{ d}^{-1}$  in sectors 59 and 53, and in both cases the amplitude is around 6 ppt.

The case of 4U 1954+319 is more peculiar, as it is a unique object. 4U 1954+31 is the only HMXB containing a late-type supergiant (Hinkle et al. 2020). The periodograms show a peak on all sectors around  $4.2 \text{ d}^{-1}$ ; however, there is significant variation (by an order of magnitude) in the amplitude of the peak between sectors or even within a sector.

#### 4.2. Parameters of the noise model

After de-trending and pre-whitening, the final light curves were obtained and the periodograms were computed for each sector. The periodograms were fit with the model described in Sect. 3.6. The noise-model parameters obtained for the mean periodogram of each source are listed in Table 3 along with indicators for the goodness of fit. The parameters obtained per sector are provided in Appendix B. The normalized light curves and the periodograms of the individual sources are available at <https://zenodo.org/uploads/14328326>.

##### 4.2.1. Main results

Figure 1 shows the histogram of the main model parameters for SGXBs and BeXBs. SGXBs display larger amplitude  $a_0$  and smaller characteristic frequencies  $f_c$  than BeXBs. The roll-off slope, that is, how fast the amplitude of the noise decreases as the frequency increases, follows a similar distribution. In general, there is a correlation between the value of the parameters and the overall luminosity, as can be seen in Fig. 2.

On the other hand, the range of values obtained for the red noise model parameters are compatible with the ones obtained in the literature for the TESS sample of OB supergiants (Bowman et al. 2019b, 2020). Figure 3 compares the main model parameters obtained from our analysis with those of single supergiant stars.

We also investigated the stability of the parameters over time. This analysis was possible because most sources have been observed in more than one sector, with time intervals between observations of a few hundred days or even years. We find that, typically, all parameters except the white noise level,  $\alpha_w$ , computed on each sector are within  $3\sigma$  of the parameter computed from the

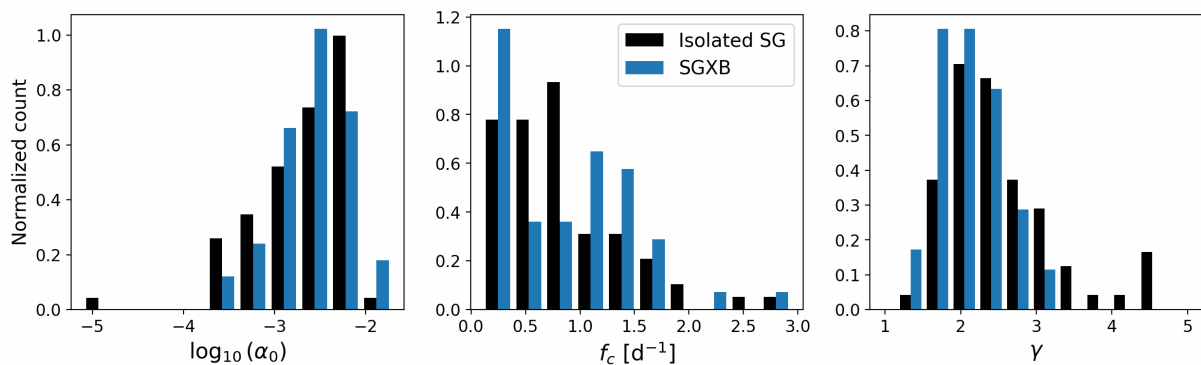


**Fig. 3.** Comparison of the best-fit SLF model parameters between SGXBs and single supergiant stars. Data for the isolated supergiants come from Bowman et al. (2019b) and Bowman et al. (2020).

mean periodogram. In terms of the root mean square, which is computed as  $rms = \sigma/av$ , where  $av$  is the average value obtained for each parameter using each individual sector of a source and  $\sigma$  is the standard deviation, the most stable parameter is  $\gamma$  with  $rms \lesssim 10\%$ , followed by  $f_c$  with  $rms \lesssim 20\%$ . For  $a_0$ , the rms varies in the range of 10–30%.

The white noise level is the parameter with the greatest dispersion. This parameter is discussed in the following section.

#### 4.2.2. White noise

There are two effects that influence the determination of the white noise level. First, high frequencies must be sampled to correctly define the noise level. Second, the intrinsic white noise is mixed with photon noise, which depends on the apparent magnitude and instrumental sensitivity (Bowman et al. 2020; Nazé et al. 2021).

As mentioned in Sect. 3.4, the time resolution of the TESS light curves changed over the course of the mission. The resolution determines the maximum frequency (Nyquist frequency) of the periodogram. To be able to use the maximum amount of data in a homogeneous way, we limited the maximum frequency to  $24 \text{ d}^{-1}$  (time resolution of 1800 s). However, for sources with a high value of  $f_c$ , as in the BeXBs, this maximum frequency proved to be insufficient, resulting in underestimated values of  $\alpha_w$ . This effect can be seen in the left panel of Fig. 4, which shows the relationship between white noise and apparent magnitude. The left panel in this figure shows the white noise computed from the periodogram. The lower noise in BeXBs can be attributed to the limited range in frequencies that defines the noise level. To account for this effect, we computed the noise level directly from the light curves, as follows: the light curves were filtered by a high-pass filter with a cut-off frequency of  $15 \text{ d}^{-1}$  to eliminate all the low-frequency components, and the variance of the residual signal was computed. This was then converted to an equivalent amplitude spectrum level  $\alpha_{HF}$ , which is expected to be close to the value of  $\alpha_w$  obtained through the periodogram fitting. Figure 4 illustrates the dependence of the white noise on the brightness of the source (i.e., photon noise). The straight line is simply the best log-linear fit to the data and shows that the correlation between white noise and brightness is statistically significant.

## 5. Discussion

The two main subcategories of HMXBs are SGXBs and BeXBs, which can be differentiated by the luminosity of the massive companion. This luminosity plays a fundamental role in char-

acterizing the fast optical variability in HMXBs. The aim of the present work is to investigate the optical variability of SGXBs on short timescales (hours to days) and to compare these systems with the related BeXBs and with various types of single supergiant stars. We took advantage of the rich data archive of the TESS mission and obtained light curves of a set of SGXBs (see Table 1). TESS light curves combine a fine time resolution of a few tens of seconds and a duration of a few tens of days, with almost no interruptions. Owing to the stochastic nature of the variability under investigation, we performed our analysis in the frequency domain.

### 5.1. Rapid optical variability of SGXBs: Main properties

The rapid optical variability of SGXBs is characterized by stochastic noise and a lack of coherent pulsation modes. The amplitude spectrum is well represented by a phenomenological model that consists of a red noise component that flattens at low frequencies. The red noise component extends up to the point where white noise dominates, typically up to  $\sim 10 \text{ d}^{-1}$ . However, the white noise level is dependent on the photon noise (i.e., brightness of the source) and the quality of the data (Fig. 4).

A general trend of  $a_0$  increasing and  $f_c$  decreasing as the luminosity increases is observed (Fig. 2). In contrast,  $\gamma$  does not exhibit any clear trend.

### 5.2. SGXBs versus BeXBs

In this work, we restricted the study of BeXBs to persistent (in X-rays) systems. A systematic study of BeXBs was presented in Reig & Fabregat (2022).

Although short-term variability is a common feature intrinsic to both SGXBs and BeXBs, the morphology of the periodograms and the amplitude of the signal is very different. In X-ray transient BeXBs, rapid variability manifests as multi-periodic oscillations. Many of the detected frequencies of the modulations are higher than the maximum allowed for rotation, which favors the interpretation that non-radial pulsations are the main driver of the fast optical variability in BeXBs (Reig & Fabregat 2022). The periodograms of BeXBs are characterized by stochastic variability on top of which coherent and quasi-periodic oscillations are superimposed. The most common pattern of variability in the periodograms of BeXBs (as well as in classical Be stars) is the existence of frequency groups, followed by isolated signals. Many transient BeXBs also display high-frequency ( $> 6 \text{ d}^{-1}$ ) signals, which can be interpreted as  $\beta$  Cephei-like pulsations. In

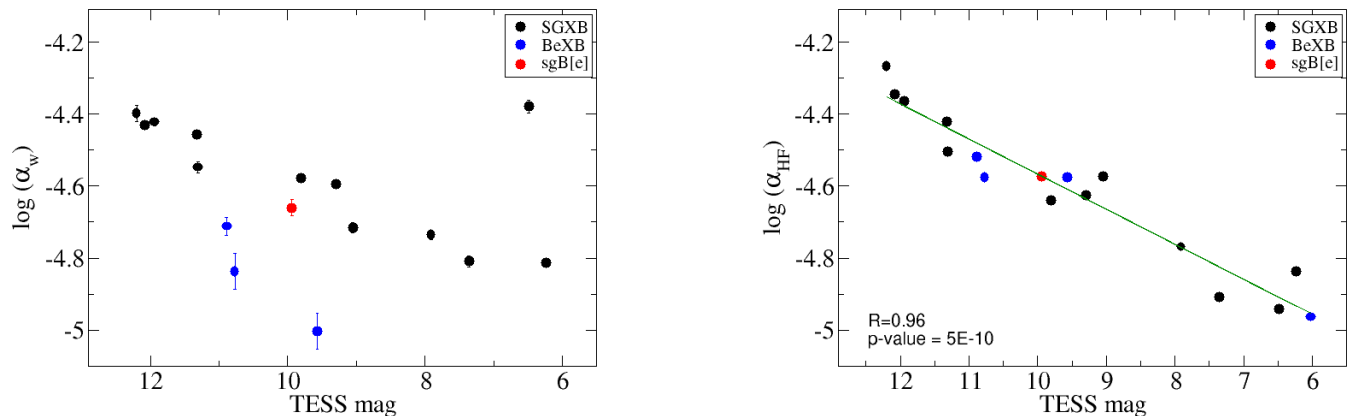


**Fig. 4.** Correlation between the white noise computed from the periodogram (left) and that derived from the light curve (right) and the apparent magnitude. Blue and black points correspond to BeXBs and SGXBs, respectively.

**Table 3.** Best-fit noise model parameters.

Source	Type	$\alpha_0/10^{-3}$	$f_c$ [ $d^{-1}$ ]	$\gamma$	$\alpha_w/10^{-5}$	$\chi^2_{red}$	$Q$
IGR J00370+6122	SGXB	$2.90 \pm 0.22$	$0.86 \pm 0.06$	$2.12 \pm 0.05$	$1.92 \pm 0.06$	1.20	3e-04
2S 0114+650	SGXB	$9.48 \pm 1.13$	$0.29 \pm 0.03$	$1.81 \pm 0.04$	$2.64 \pm 0.07$	0.93	0.910
Vela X-1	SGXB	$7.68 \pm 0.96$	$0.37 \pm 0.05$	$1.63 \pm 0.05$	$4.18 \pm 0.17$	1.02	0.340
Cen X-3	SGXB	$0.90 \pm 0.06$	$1.47 \pm 0.09$	$2.31 \pm 0.10$	$3.72 \pm 0.08$	1.26	8e-06
1E 1145.1-6141	SGXB	$4.15 \pm 0.48$	$0.33 \pm 0.03$	$1.91 \pm 0.05$	$3.50 \pm 0.06$	1.17	0.002
4U 1538-522	SGXB	$1.92 \pm 0.18$	$0.90 \pm 0.07$	$2.30 \pm 0.09$	$3.78 \pm 0.09$	1.03	0.310
4U 1700-377	SGXB	$1.79 \pm 0.12$	$1.58 \pm 0.07$	$2.81 \pm 0.08$	$1.53 \pm 0.04$	0.96	0.750
Cyg X-1	SGXB	$2.37 \pm 0.14$	$1.10 \pm 0.06$	$2.21 \pm 0.05$	$1.84 \pm 0.05$	1.09	0.056
IGR J08408-4503	SFXT	$2.12 \pm 0.12$	$1.33 \pm 0.07$	$2.21 \pm 0.05$	$1.55 \pm 0.06$	1.08	0.085
IGR J11215-5952	SFXT	$8.34 \pm 1.12$	$0.29 \pm 0.03$	$1.87 \pm 0.04$	$2.54 \pm 0.06$	0.91	0.950
IGR J16465-4507	SFXT	$0.39 \pm 0.03$	$2.02 \pm 0.22$	$1.81 \pm 0.14$	$4.00 \pm 0.20$	1.05	0.200
XTE J1739-302	SFXT	$1.24 \pm 0.19$	$1.25 \pm 0.14$	$3.02 \pm 0.25$	$2.83 \pm 0.10$	1.11	0.030
RX J0146.9+6121	BeXB	$0.52 \pm 0.09$	$1.35 \pm 0.28$	$1.80 \pm 0.18$	$1.46 \pm 0.17$	1.10	0.040
X Per	BeXB	$0.42 \pm 0.02$	$2.73 \pm 0.12$	$2.14 \pm 0.07$	$0.72 \pm 0.06$	1.50	3e-15
4U 1036-56	BeXB	$1.25 \pm 0.08$	$1.44 \pm 0.10$	$1.85 \pm 0.06$	$1.94 \pm 0.11$	1.19	8e-04
4U 2206+543	BeXB	$1.06 \pm 0.06$	$1.97 \pm 0.12$	$1.94 \pm 0.06$	$0.99 \pm 0.11$	1.15	0.004
XTE J0421+560	sgB[e]	$3.43 \pm 0.51$	$0.39 \pm 0.06$	$1.57 \pm 0.06$	$2.19 \pm 0.11$	1.09	0.051
4U 1954+319	sg(M)	$0.14 \pm 0.01$	$1.66 \pm 0.30$	$0.99 \pm 0.09$	$0.43 \pm 0.18$	1.79	2e-31

**Notes.** Columns 3-6 give the amplitude of the SLF variability, its characteristic frequency, the roll-off slope in logarithmic scale, and the white noise level. Columns 7-8 provide the goodness of fit through the reduced  $\chi^2$  and probability  $Q$ . Typically, a fit is considered to be good if  $\chi^2_{red} \approx 1$  or  $Q > 0.001$ .

contrast, the pulsational content in SGXBs is very scarce and completely absent above  $2 d^{-1}$  (Table 2).

The stochastic variability between SGXBs and BeXBs is also different. While in SGXBs, SLF variability is characterized by red noise and flattens toward lower frequencies, in BeXBs the low-frequency part of the periodogram also exhibits a red-noise-like component, but in this case, it is made up of a forest of signals whose origin is believed to be inhomogeneities in the inner circumstellar disk and/or light outbursts (Reig & Fabregat 2022). The differences between SGXBs and BeXBs are also notorious even when considering persistent BeXBs, as can be seen in Fig. 2.

### 5.3. SGXBs versus single supergiant stars

Similarly to the relationship between BeXBs and classical Be stars, the rapid optical variability of SGXBs is very similar to that of isolated supergiant stars. The range of values obtained for the red noise model parameters is compatible with that found in the literature for isolated supergiants (Bowman et al. 2019b, 2020; Dorn-Wallenstein et al. 2020; Nazé et al. 2021). In particular, the logarithmic amplitude gradient  $\gamma$  varies typically in a range between 1.5 and 3.5, with a higher concentration around  $\gamma = 2$ , while the characteristic frequency is distributed mainly below  $1.5 d^{-1}$  (see Fig. 3). Likewise, the dependence between the noise parameters and the luminosity described in Sect. 5.1 also agrees with the results of Bowman et al. (2019b), who found a similar correlation in their TESS sample of supergiant stars in the Large Magellanic Cloud.



The lack of significant frequencies among SGXBs is in line with the results presented in Bowman et al. (2019b), where among the type Ia supergiants all but one show a frequency spectrum containing mainly red noise without any other peaks. Among the sample of 91 supergiants, only two show  $\beta$  Cephei-like pulsations, and both are type Ib.

In our sample of SGXBs, only IGR J16465-4507 shows a  $\beta$  Cephei-like pulsation. IGR J16465-4507 was classified as type B0.5-1Ib by Chaty et al. (2016), who also obtained the values of  $T_{\text{eff}} = 26\,000$  K and  $\log g = 3.1$  from spectral modeling. These parameters place the star within the boundaries of the theoretical  $\beta$  Cephei instability strip (Pamyatnykh 1999). Another peculiarity of this source is its high rotational speed, estimated at  $320 \text{ km s}^{-1}$  (Chaty et al. 2016). This value is significantly higher than typical values in SGXBs (Liu et al. 2006). Moreover, H $\alpha$  emission is also observed, which led Chaty et al. (2016) to speculate that it may come from circumstellar material, possibly with a disk-like geometry. Finally, its position on the Corbet diagram places it between Be and supergiant systems, and therefore it is possibly a descendant of BeXBs. In view of these facts, it is not surprising that our analysis reveals that the best-fit noise model parameters of IGR J16465-4507 are more aligned with those of BeXBs than those of SGXBs.

#### 5.4. Origin of the variability

The physical cause of the SLF variability in early-type massive stars is unclear. Internal gravity waves (IGWs) excited by core convection have been proposed to explain this low-frequency variability (Rogers et al. 2013; Aerts & Rogers 2015; Edelman et al. 2019; Bowman et al. 2019b; Ratnasingam et al. 2020, 2023; Vanon et al. 2023; Herwig et al. 2023; Thompson et al. 2024). However, other authors, such as Lecoanet et al. (2019) and Cantiello et al. (2021), argue that the observed low-frequency variability in massive stars is unlikely to be due to internal gravity waves generated by core convection, because they would suffer strong radiative damping toward the surface, resulting in very little surface luminosity variation (see also Anders et al. 2023). Instead, these authors attribute the presence of red noise to subsurface convection zones driven by the iron opacity peak.

The models disagree even in the interpretation of the observations. Bowman et al. (2019b) claimed that the correlation between  $\alpha_0$  and brightness supports the interpretation that the SLF variability observed in OB stars is evidence of IGWs, arguing that the amplitudes of individual waves caused by core convection are predicted to scale with the local core luminosity, and therefore the mass of the convective core. In contrast, Cantiello et al. (2021) argued that this correlation should go in the opposite direction, because IGWs are expected to have a weaker influence toward higher luminosities. Also, the predicted characteristic frequencies expected to result from IGWs are significantly smaller than those observed (Shiode et al. 2013; Cantiello et al. 2021). Finally, the correlation between the characteristic frequency and luminosity (Fig. 2) would also be at odds with the SLF variability being due to IGWs because the characteristic frequencies of peak IGWs should increase as stars evolve on the main sequence (Cantiello et al. 2021), which is the opposite of what is observed.

Owing to the complexity of the problem, analytical models make some simplifying assumptions (e.g., mixing-length theory, non-rotating models, linear wave propagation, and no wave-wave interaction), which limit our ability to make accurate comparisons to observations, especially for massive evolved stars.

Studies of the excitation and propagation of gravity waves have greatly benefited from 3D hydrodynamic simulations in recent years, which allow the inclusion of those simplifying assumptions, and coverage of a significant fraction of the star's radius, but these simulations have not solved the controversy. Many hydrodynamic simulations appear to validate the effectiveness of IGWs in explaining the SLF variability and are qualitatively consistent with observations (Edelmann et al. 2019; Ratnasingam et al. 2023; Vanon et al. 2023; Herwig et al. 2023; Thompson et al. 2024). In contrast, other models that simulate gravity waves driven by core convection predict that the photometric variability due to those waves is orders of magnitude lower than the observed variability (Anders et al. 2023).

In either case, these models remain to be applied to more evolved stars (i.e., supergiants). From stellar evolution theory, it is expected that the size of the subsurface convection zone grows as stars evolve. Hence, the contribution to SLF variability from subsurface convection zones may be the dominant process in supergiant stars (Bowman & Dorn-Wallenstein 2022). On the other hand, the role of inhomogeneities in the stellar surface or in the wind, in combination with rotation (Aerts et al. 2017; Simón-Díaz et al. 2018; Krтіčka & Feldmeier 2021), must also be taken into account.

## 6. Conclusion

We studied the rapid optical variability of the massive counterparts in SGXBs. We show that most of the power in the periodograms of SGXBs is not caused by pulsation but by SLF variability. When this variability is described by a phenomenological model, the parameters of the model that describe the amplitude at zero frequency  $a_0$  and the logarithmic amplitude gradient (i.e., the slope of the linear decrease)  $\gamma$  appear to depend on luminosity (Fig. 2). More luminous sources tend to show variability of greater amplitude and lower logarithmic amplitude gradients than less luminous sources. The statistical significance of this trend should be assessed when reliable values of the luminosity become available. The specific physical cause of this noise remains unclear. Such low-frequency variability could be produced by a combination of internal gravity waves excited at the interface between the convective core and the radiative envelope or in a subsurface convection zone.

The amplitude spectra of SGXBs and BeXBs display very different components. In terms of the pulsational content, the main difference is the disappearance of coherent signals as the luminosity increases. In terms of the SLF variability, in SGXBs, the amplitude  $a_0$  and the characteristic frequency  $f_c$  (i.e., the characteristic variability timescale) decrease as the luminosity increases.

## 7. Data availability

The light curves and periodograms of individual sources are available on the Zenodo repository: <https://zenodo.org/uploads/14328326>

*Acknowledgements.* We thank the anonymous referee for his/her useful comments. This paper includes data collected by the TESS mission. Funding for the TESS mission is provided by the NASA's Science Mission Directorate. This research has made use of the SIMBAD database, operated at CDS, Strasbourg, France and of NASA's Astrophysics Data System operated by the Smithsonian Astrophysical Observatory.

## References

- Aerts, C. 2021, *Reviews of Modern Physics*, 93, 015001
- Aerts, C. & Rogers, T. M. 2015, *ApJ*, 806, L33
- Aerts, C., Simón-Díaz, S., Bloemen, S., et al. 2017, *A&A*, 602, A32
- Anders, E. H., Lecoanet, D., Cantiello, M., et al. 2023, *Nature Astronomy*, 7, 1228
- Baade, D. 1984, *A&A*, 134, 105
- Baade, D., Pigulski, A., Rivinius, T., et al. 2018, *A&A*, 620, A145
- Baade, D., Rivinius, T., Pigulski, A., et al. 2016, *A&A*, 588, A56
- Balona, L. A. 2003, *Ap&SS*, 284, 121
- Balona, L. A. & Ozuyar, D. 2020, *MNRAS*, 493, 2528
- Balona, L. A. & Ozuyar, D. 2021, *ApJ*, 921, 5
- Blomme, R., Mahy, L., Catala, C., et al. 2011, *A&A*, 533, A4
- Bowman, D. M. 2023, *Ap&SS*, 368, 107
- Bowman, D. M., Aerts, C., Johnston, C., et al. 2019a, *A&A*, 621, A135
- Bowman, D. M., Burssens, S., Pedersen, M. G., et al. 2019b, *Nature Astronomy*, 3, 760
- Bowman, D. M., Burssens, S., Simón-Díaz, S., et al. 2020, *A&A*, 640, A36
- Bowman, D. M. & Dorn-Wallenstein, T. Z. 2022, *A&A*, 668, A134
- Bowman, D. M. & Michielsen, M. 2021, *A&A*, 656, A158
- Brasseur, C. E., Phillip, C., Hargis, J., et al. 2019, in *Astronomical Society of the Pacific Conference Series*, Vol. 523, *Astronomical Data Analysis Software and Systems XXVII*, ed. P. J. Teuben, M. W. Pound, B. A. Thomas, & E. M. Warner, 397
- Burssens, S., Simón-Díaz, S., Bowman, D. M., et al. 2020, *A&A*, 639, A81
- Cantiello, M., Lecoanet, D., Jermyn, A. S., & Grassitelli, L. 2021, *ApJ*, 915, 112
- Chaty, S., LeReun, A., Negueruela, I., et al. 2016, *A&A*, 591, A87
- Corbet, R. H. D. 1986, *MNRAS*, 220, 1047
- Dorn-Wallenstein, T. Z., Levesque, E. M., & Davenport, J. R. A. 2019, *ApJ*, 878, 155
- Dorn-Wallenstein, T. Z., Levesque, E. M., Neugent, K. F., et al. 2020, *ApJ*, 902, 24
- Edelmann, P. V. F., Ratnasingam, R. P., Pedersen, M. G., et al. 2019, *ApJ*, 876, 4
- Fortin, F., García, F., Simaz Bunzel, A., & Chaty, S. 2023, *A&A*, 671, A149
- Herwig, F., Woodward, P. R., Mao, H., et al. 2023, *MNRAS*, 525, 1601
- Hinkle, K. H., Lebzelter, T., Fekel, F. C., et al. 2020, *ApJ*, 904, 143
- Kim, V., Izmailova, I., & Aimuratov, Y. 2023, *ApJS*, 268, 21
- Koch, D. G., Borucki, W. J., Basri, G., et al. 2010, *ApJ*, 713, L79
- Kretschmar, P., El Mellah, I., Martínez-Núñez, S., et al. 2021, *A&A*, 652, A95
- Kretschmar, P., Fürst, F., Sidoli, L., et al. 2019, *New A Rev.*, 86, 101546
- Krtićka, J. & Feldmeier, A. 2021, *A&A*, 648, A79
- Lecoanet, D., Cantiello, M., Quataert, E., et al. 2019, *ApJ*, 886, L15
- Lenoir-Craig, G., St-Louis, N., Moffat, A. F. J., et al. 2022, *ApJ*, 925, 79
- Lightkurve Collaboration, Cardoso, J. V. d. M., Hedges, C., et al. 2018, *Lightkurve: Kepler and TESS time series analysis in Python*, *Astrophysics Source Code Library*
- Liu, Q. Z., van Paradijs, J., & van den Heuvel, E. P. J. 2006, *A&A*, 455, 1165
- Martínez-Núñez, S., Kretschmar, P., Bozzo, E., et al. 2017, *Space Sci. Rev.*, 212, 59
- Nazé, Y., Rauw, G., & Gosset, E. 2021, *MNRAS*, 502, 5038
- Negueruela, I., Smith, D. M., Reig, P., Chaty, S., & Torrejón, J. M. 2006, in *ESA Special Publication*, Vol. 604, *The X-ray Universe 2005*, ed. A. Wilson, 165
- Neumann, M., Avakyan, A., Doroshenko, V., & Santangelo, A. 2023, *A&A*, 677, A134
- Pamyatnykh, A. A. 1999, *Acta Astron.*, 49, 119
- Paul, B. & Naik, S. 2011, *Bulletin of the Astronomical Society of India*, 39, 429
- Porter, J. M. & Rivinius, T. 2003, *PASP*, 115, 1153
- Press, W. H., Teukolsky, S. A., Vetterling, W. T., et al. 1993, *The Observatory*, 113, 214
- Ratnasingam, R. P., Edelmann, P. V. F., & Rogers, T. M. 2020, *MNRAS*, 497, 4231
- Ratnasingam, R. P., Rogers, T. M., Chowdhury, S., et al. 2023, *A&A*, 674, A134
- Reig, P. 2011, *Ap&SS*, 332, 1
- Reig, P. & Fabregat, J. 2022, *A&A*, 667, A18
- Reig, P. & Roche, P. 1999, *MNRAS*, 306, 100
- Ricker, G. R., Winn, J. N., Vanderspek, R., et al. 2015, *Journal of Astronomical Telescopes, Instruments, and Systems*, 1, 014003
- Rivinius, T., Baade, D., & Carciofi, A. C. 2016, *A&A*, 593, A106
- Rivinius, T., Baade, D., Stefl, S., et al. 1998, *A&A*, 336, 177
- Rivinius, T., Baade, D., & Stefl, S. 2003, *A&A*, 411, 229
- Rivinius, T., Carciofi, A. C., & Martayan, C. 2013, *A&A Rev.*, 21, 69
- Rogers, T. M., Lin, D. N. C., McElwaine, J. N., & Lau, H. H. B. 2013, *ApJ*, 772, 21
- Semaan, T., Hubert, A. M., Zorec, J., et al. 2018, *A&A*, 613, A70
- Shiode, J. H., Quataert, E., Cantiello, M., & Bildsten, L. 2013, *MNRAS*, 430, 1736
- Simón-Díaz, S., Aerts, C., Urbaneja, M. A., et al. 2018, *A&A*, 612, A40
- Stanishev, V., Kraicheva, Z., Boffin, H. M. J., & Genkov, V. 2002, *A&A*, 394, 625
- Thompson, W., Herwig, F., Woodward, P. R., et al. 2024, *MNRAS*, 531, 1316
- Tkachenko, A., Degroote, P., Aerts, C., et al. 2014, *MNRAS*, 438, 3093
- van Paradijs, J., Lub, J., Pel, J. W., Pakull, M., & van Amerongen, S. 1983, *A&A*, 124, 294
- Vanon, R., Edelmann, P. V. F., Ratnasingam, R. P., Varghese, A., & Rogers, T. M. 2023, *ApJ*, 954, 171
- Zima, W. 2006, *A&A*, 455, 227

**Appendix A: Significant independent frequencies**

Independent frequencies of the different types of sources.

**Table A.1.** Significant frequencies - SGXBs.

	Frequency [d <sup>-1</sup> ]	Amplitude [ppt]	SNR
Vela X-1			
Sector 8	0.220	32.48	5.1
	0.122	16.59	5.2
Sector 9	0.217	26.63	5.9
	0.174	12.12	4.6
Sector 35	None		
Sector 62	0.225	31.37	5.2
	0.133	15.90	4.0
Cen X-3			
Sector 10	0.959	21.98	26.3
	1.435	2.95	6.0
Sector 11	0.957	20.85	38.8
	1.440	2.80	6.6
	0.484	3.77	4.8
Sector 37	0.958	17.69	28.3
	1.437	2.67	7.2
Sector 64	0.958	18.25	26.1
	1.428	1.97	4.5
	3.834	0.62	4.3
4U 1538-522			
Sector 12	0.536	12.16	10.0
Sector 39	0.533	9.99	11.4
Sector 65	0.540	11.83	10.9
4U 1700-377			
Sector 12	0.589	13.78	10.0
Sector 39	0.587	15.44	10.3
Sector 66	0.584	13.32	6.2
Cyg X-1			
Sector 14	0.371	14.46	5.4
Sector 54	0.356	17.27	9.4
	0.188	8.23	5.0
Sector 55	0.359	17.08	9.5
Sector 74	0.355	20.98	12.6
Sector 75	0.371	13.09	5.2
	2.337	1.46	4.8
IGR J08408-4503			
Sector 8	None		
Sector 9	None		
Sector 35	0.271	13.49	5.0
Sector 61	0.275	11.90	5.0
Sector 62	0.275	9.87	7.8
IGR J16465-4507			
Sector 12	7.374	7.22	74.4
	14.750	0.78	10.4
Sector 39	7.374	9.35	114.1
	14.749	1.08	19.9
	22.131	0.27	5.4
Sector 66	7.374	7.16	88.2
	14.748	0.83	16.2
	22.123	0.25	5.7

**Table A.2.** Significant frequencies - BeXBs.

	Frequency [d <sup>-1</sup> ]	Amplitude [ppt]	SNR
RX J0146.9+6121			
Sector 58	9.680	1.53	35.6
	13.293	0.64	22.1
	14.282	0.35	12.5
	2.923	1.92	12.8
	8.417	0.32	8.2
	22.966	0.14	6.3
	15.265	0.16	5.8
	1.502	1.97	5.8
	16.719	0.12	5.1
	2.885	0.67	5.0
	17.884	0.11	4.5
4U 1036-56			
Sector 10	4.912	0.85	5.3
	5.647	0.50	4.3
	1.851	1.85	4.1
Sector 36	4.910	0.77	4.3
Sector 37	4.917	1.07	5.7
	1.874	2.70	5.6
4U 2206+543			
Sector 16	6.143	0.78	5.8
Sector 17	6.136	0.86	6.1
Sector 56	6.138	0.72	5.2
Sector 57	6.135	0.88	6.5
X Per			
Sector 18	3.607	1.90	9.0
	1.742	2.74	10.0
	8.626	0.38	8.2
	3.686	1.27	6.8
	10.410	0.20	5.8
	1.923	1.12	4.4
	3.841	0.79	4.5
Sector 43	1.738	3.42	9.0
	3.614	2.14	8.9
	2.885	1.88	7.0
	3.679	1.50	7.0
	3.836	1.12	5.4
	10.368	0.15	4.3
	8.635	0.21	4.3
Sector 44	3.612	3.72	15.1
	2.886	2.00	6.8
	1.832	2.49	5.7
	1.723	2.43	5.7
	3.837	0.95	4.2
	3.664	0.90	4.2
Sector 70	6.793	0.70	15.5
	13.588	0.21	12.2
	1.216	2.26	12.8
	3.526	1.02	9.2
	3.634	0.93	8.5
	20.383	0.08	7.8
	3.679	0.78	7.0
	3.741	0.65	5.9
	6.497	0.25	5.6
	7.092	0.24	5.6
	3.815	0.57	5.4
	11.592	0.10	4.5
Sector 71	3.623	1.71	12.2
	3.665	1.11	8.1
	1.218	1.98	10.5
	3.841	0.89	6.9
	3.503	0.76	5.9
	3.731	0.64	5.2
	7.086	0.19	4.3

**Table A.3.** Significant frequencies - Others.

	Frequency [d <sup>-1</sup> ]	Amplitude [ppt]	SNR
<b>XTE J0421+560</b>			
Sector 19	2.466	7.37	28.8
Sector 59	2.466	6.64	29.6
	1.097	5.34	10.9
Sector 73	2.467	5.41	17.7
	1.096	5.88	10.7
<b>4U 1954+319</b>			
Sector 14	4.354	0.30	10.0
	12.104	0.10	4.4
Sector 41	4.258	3.04	26.4
	8.515	1.14	15.9
	4.205	0.82	7.2
	12.752	0.24	5.3
	4.324	0.55	5.0
	8.578	0.33	4.7
	4.405	0.49	4.5
	17.495	0.15	4.1
Sector 54	4.201	0.32	5.8
Sector 55	4.195	0.37	18.1
	8.381	0.09	6.9
	4.238	0.13	6.3
	4.284	0.10	4.8
	8.440	0.05	4.1
Sector 74	4.202	0.70	22.2
	8.407	0.33	19.2
	8.441	0.20	11.8
	4.236	0.31	10.7
	8.364	0.13	8.0
	12.625	0.06	5.6
Sector 75	4.247	0.96	33.6
	8.492	0.54	32.1
	21.250	0.09	9.9
	12.743	0.09	7.7
	8.524	0.12	7.5
	16.979	0.06	6.2

**Appendix B: Results per sector**

The following table presents the best-fit noise model obtained for each sector of each source as well as for its mean periodogram, grouped by source type.

**Table B.1.** Noise model parameters - SGXBs.

Source	Sector	$\alpha_0/10^{-3}$	$f_c$ [d $^{-1}$ ]	$\gamma$	$\alpha_w/10^{-5}$	$\chi_{red}^2$
IGR J00370+6122	17	$3.75 \pm 0.79$	$0.68 \pm 0.12$	$2.06 \pm 0.12$	$2.19 \pm 0.15$	1.08
IGR J00370+6122	18	$2.33 \pm 0.43$	$0.92 \pm 0.15$	$2.10 \pm 0.14$	$2.03 \pm 0.15$	1.04
IGR J00370+6122	24	$1.92 \pm 0.34$	$1.00 \pm 0.16$	$2.14 \pm 0.14$	$1.75 \pm 0.13$	0.93
IGR J00370+6122	58	$2.12 \pm 0.36$	$1.00 \pm 0.13$	$2.31 \pm 0.12$	$0.96 \pm 0.07$	0.95
IGR J00370+6122	Mean	$2.90 \pm 0.22$	$0.86 \pm 0.06$	$2.12 \pm 0.05$	$1.92 \pm 0.06$	1.20
2S 0114+650	18	$13.24 \pm 5.74$	$0.17 \pm 0.07$	$1.57 \pm 0.09$	$2.49 \pm 0.24$	0.93
2S 0114+650	24	$8.99 \pm 2.67$	$0.33 \pm 0.08$	$1.94 \pm 0.11$	$2.74 \pm 0.16$	1.10
2S 0114+650	25	$5.24 \pm 1.50$	$0.37 \pm 0.09$	$1.86 \pm 0.11$	$1.85 \pm 0.13$	0.90
2S 0114+650	52	$6.44 \pm 2.08$	$0.30 \pm 0.08$	$1.76 \pm 0.10$	$1.87 \pm 0.14$	0.87
2S 0114+650	58	$8.53 \pm 2.45$	$0.35 \pm 0.08$	$2.06 \pm 0.12$	$2.96 \pm 0.15$	0.32
2S 0114+650	Mean	$9.48 \pm 1.13$	$0.29 \pm 0.03$	$1.81 \pm 0.04$	$2.64 \pm 0.07$	0.93
Vela X-1	8	$6.84 \pm 2.18$	$0.38 \pm 0.14$	$1.46 \pm 0.12$	$5.45 \pm 0.70$	0.92
Vela X-1	9	$4.66 \pm 1.36$	$0.43 \pm 0.13$	$1.54 \pm 0.12$	$3.06 \pm 0.38$	0.80
Vela X-1	35	$7.81 \pm 2.25$	$0.38 \pm 0.10$	$1.76 \pm 0.11$	$3.53 \pm 0.28$	1.01
Vela X-1	62	$7.54 \pm 2.21$	$0.36 \pm 0.09$	$1.81 \pm 0.10$	$2.46 \pm 0.19$	0.46
Vela X-1	Mean	$7.68 \pm 0.96$	$0.37 \pm 0.05$	$1.63 \pm 0.05$	$4.18 \pm 0.17$	1.02
Cen X-3	10	$0.98 \pm 0.18$	$1.18 \pm 0.22$	$2.09 \pm 0.21$	$3.57 \pm 0.21$	0.91
Cen X-3	11	$0.60 \pm 0.08$	$2.12 \pm 0.25$	$2.72 \pm 0.29$	$3.53 \pm 0.17$	1.08
Cen X-3	37	$0.75 \pm 0.12$	$1.36 \pm 0.22$	$2.23 \pm 0.21$	$2.65 \pm 0.15$	0.98
Cen X-3	64	$0.72 \pm 0.10$	$1.68 \pm 0.22$	$2.64 \pm 0.27$	$3.47 \pm 0.16$	1.03
Cen X-3	Mean	$0.90 \pm 0.06$	$1.47 \pm 0.09$	$2.31 \pm 0.10$	$3.72 \pm 0.08$	1.26
1E 1145.1-6141	10	$3.08 \pm 0.87$	$0.39 \pm 0.10$	$2.10 \pm 0.18$	$3.69 \pm 0.15$	1.01
1E 1145.1-6141	11	$3.62 \pm 1.05$	$0.35 \pm 0.08$	$2.11 \pm 0.15$	$2.48 \pm 0.10$	1.14
1E 1145.1-6141	37	$3.28 \pm 1.07$	$0.31 \pm 0.10$	$1.75 \pm 0.13$	$2.44 \pm 0.14$	0.86
1E 1145.1-6141	38	$4.33 \pm 1.44$	$0.29 \pm 0.09$	$1.87 \pm 0.14$	$3.30 \pm 0.15$	1.02
1E 1145.1-6141	64	$4.56 \pm 1.55$	$0.28 \pm 0.09$	$1.80 \pm 0.14$	$3.36 \pm 0.17$	0.96
1E 1145.1-6141	Mean	$4.15 \pm 0.48$	$0.33 \pm 0.03$	$1.91 \pm 0.05$	$3.50 \pm 0.06$	1.17
4U 1538-522	12	$1.31 \pm 0.21$	$1.18 \pm 0.16$	$2.62 \pm 0.23$	$3.60 \pm 0.15$	1.16
4U 1538-522	39	$1.64 \pm 0.30$	$0.93 \pm 0.15$	$2.32 \pm 0.19$	$3.33 \pm 0.16$	1.06
4U 1538-522	65	$1.97 \pm 0.40$	$0.79 \pm 0.14$	$2.16 \pm 0.17$	$3.05 \pm 0.16$	0.98
4U 1538-522	Mean	$1.92 \pm 0.18$	$0.90 \pm 0.07$	$2.30 \pm 0.09$	$3.78 \pm 0.09$	1.03
4U 1700-377	12	$1.41 \pm 0.19$	$1.62 \pm 0.17$	$2.75 \pm 0.17$	$1.75 \pm 0.10$	0.90
4U 1700-377	39	$1.49 \pm 0.19$	$1.72 \pm 0.15$	$2.99 \pm 0.17$	$1.43 \pm 0.07$	0.92
4U 1700-377	66	$2.04 \pm 0.29$	$1.31 \pm 0.14$	$2.64 \pm 0.13$	$1.07 \pm 0.07$	0.79
4U 1700-377	Mean	$1.79 \pm 0.12$	$1.58 \pm 0.07$	$2.81 \pm 0.08$	$1.53 \pm 0.04$	0.96
Cyg X-1	14	$2.32 \pm 0.44$	$0.92 \pm 0.16$	$1.96 \pm 0.13$	$1.91 \pm 0.19$	1.08
Cyg X-1	54	$1.87 \pm 0.27$	$1.33 \pm 0.15$	$2.50 \pm 0.15$	$1.58 \pm 0.10$	1.03
Cyg X-1	55	$2.06 \pm 0.32$	$1.17 \pm 0.14$	$2.42 \pm 0.13$	$1.07 \pm 0.08$	1.01
Cyg X-1	74	$1.78 \pm 0.28$	$1.23 \pm 0.17$	$2.23 \pm 0.14$	$1.62 \pm 0.13$	0.88
Cyg X-1	75	$2.13 \pm 0.38$	$1.01 \pm 0.17$	$2.03 \pm 0.13$	$1.81 \pm 0.17$	0.64
Cyg X-1	Mean	$2.37 \pm 0.14$	$1.10 \pm 0.06$	$2.21 \pm 0.05$	$1.84 \pm 0.05$	1.09

**Table B.2.** Noise model parameters - SFXTs.

Source	Sector	$\alpha_0/10^{-3}$	$f_c$ [d $^{-1}$ ]	$\gamma$	$\alpha_w/10^{-5}$	$\chi_{red}^2$
IGR J08408-4503	8	1.98 ± 0.33	1.20 ± 0.19	2.03 ± 0.14	1.95 ± 0.21	0.91
IGR J08408-4503	9	1.36 ± 0.18	1.63 ± 0.18	2.54 ± 0.16	1.48 ± 0.10	1.07
IGR J08408-4503	35	2.80 ± 0.49	1.05 ± 0.17	2.05 ± 0.13	2.03 ± 0.21	0.87
IGR J08408-4503	61	1.70 ± 0.24	1.45 ± 0.16	2.33 ± 0.11	0.41 ± 0.07	0.88
IGR J08408-4503	62	1.53 ± 0.22	1.47 ± 0.18	2.29 ± 0.14	1.18 ± 0.12	0.75
IGR J08408-4503	Mean	2.12 ± 0.12	1.33 ± 0.07	2.21 ± 0.05	1.55 ± 0.06	1.08
IGR J11215-5952	10	4.96 ± 1.46	0.36 ± 0.09	1.81 ± 0.11	2.33 ± 0.16	0.94
IGR J11215-5952	11	19.52 ± 11.17	0.10 ± 0.05	1.60 ± 0.09	1.91 ± 0.15	0.65
IGR J11215-5952	37	7.63 ± 2.35	0.30 ± 0.07	2.01 ± 0.11	1.75 ± 0.09	0.89
IGR J11215-5952	64	4.17 ± 0.89	0.63 ± 0.10	2.38 ± 0.16	3.22 ± 0.14	0.98
IGR J11215-5952	Mean	8.34 ± 1.12	0.29 ± 0.03	1.87 ± 0.04	2.54 ± 0.06	0.91
IGR J16465-4507	12	0.53 ± 0.11	1.40 ± 0.36	1.74 ± 0.26	4.41 ± 0.37	1.05
IGR J16465-4507	39	0.27 ± 0.04	2.94 ± 0.43	2.39 ± 0.38	3.88 ± 0.27	1.03
IGR J16465-4507	66	0.36 ± 0.09	1.45 ± 0.58	1.23 ± 0.24	1.81 ± 0.61	0.94
IGR J16465-4507	Mean	0.39 ± 0.03	2.02 ± 0.22	1.81 ± 0.14	4.00 ± 0.20	1.05
XTE J1739-302	39	1.24 ± 0.19	1.25 ± 0.14	3.02 ± 0.25	2.83 ± 0.10	1.11

**Table B.3.** Noise model parameters - BeXBs.

Source	Sector	$\alpha_0/10^{-3}$	$f_c$ [d $^{-1}$ ]	$\gamma$	$\alpha_w/10^{-5}$	$\chi_{red}^2$
RX J0146.9+6121	58	0.52 ± 0.09	1.35 ± 0.28	1.80 ± 0.18	1.46 ± 0.17	1.10
X Per	18	0.28 ± 0.03	3.66 ± 0.35	2.55 ± 0.23	0.84 ± 0.12	0.98
X Per	43	0.46 ± 0.06	2.59 ± 0.33	2.16 ± 0.20	1.11 ± 0.17	0.94
X Per	44	0.64 ± 0.08	2.32 ± 0.29	2.17 ± 0.17	0.81 ± 0.15	0.83
X Per	70	0.31 ± 0.06	1.54 ± 0.40	1.45 ± 0.17	0.34 ± 0.20	1.08
X Per	71	0.28 ± 0.04	2.41 ± 0.37	1.81 ± 0.15	0.00 ± 0.11	1.26
X Per	Mean	0.42 ± 0.02	2.73 ± 0.12	2.14 ± 0.07	0.72 ± 0.06	1.50
4U 1036-56	10	0.99 ± 0.17	1.35 ± 0.28	1.70 ± 0.15	1.40 ± 0.28	1.07
4U 1036-56	36	0.86 ± 0.12	1.89 ± 0.29	2.04 ± 0.19	2.39 ± 0.27	0.94
4U 1036-56	37	1.29 ± 0.22	1.32 ± 0.25	1.83 ± 0.16	2.05 ± 0.28	0.99
4U 1036-56	63	1.11 ± 0.17	1.50 ± 0.24	1.95 ± 0.15	1.22 ± 0.19	1.13
4U 1036-56	64	1.25 ± 0.22	1.21 ± 0.24	1.78 ± 0.14	1.38 ± 0.24	1.08
4U 1036-56	Mean	1.25 ± 0.08	1.44 ± 0.10	1.85 ± 0.06	1.94 ± 0.11	1.19
4U 2206+543	16	1.04 ± 0.15	1.76 ± 0.28	1.85 ± 0.14	0.71 ± 0.25	0.96
4U 2206+543	17	1.03 ± 0.15	1.89 ± 0.27	2.08 ± 0.18	2.15 ± 0.26	0.84
4U 2206+543	56	0.75 ± 0.09	2.51 ± 0.31	2.09 ± 0.15	0.44 ± 0.20	1.07
4U 2206+543	57	0.91 ± 0.13	1.95 ± 0.30	1.84 ± 0.14	0.30 ± 0.24	1.04
4U 2206+543	Mean	1.06 ± 0.06	1.97 ± 0.12	1.94 ± 0.06	0.99 ± 0.11	1.15

**Table B.4.** Noise model parameters - Others.

Source	Sector	$\alpha_0/10^{-3}$	$f_c$ [d $^{-1}$ ]	$\gamma$	$\alpha_w/10^{-5}$	$\chi_{red}^2$
XTE J0421+560	19	3.25 ± 0.94	0.41 ± 0.12	1.68 ± 0.12	2.27 ± 0.19	0.99
XTE J0421+560	59	3.40 ± 1.07	0.34 ± 0.11	1.61 ± 0.11	1.85 ± 0.17	0.91
XTE J0421+560	73	2.65 ± 0.80	0.42 ± 0.14	1.46 ± 0.12	1.72 ± 0.27	0.90
XTE J0421+560	Mean	3.43 ± 0.51	0.39 ± 0.06	1.57 ± 0.06	2.19 ± 0.11	1.09
4U 1954+319	14	0.11 ± 0.03	1.00 ± 0.41	1.50 ± 0.33	1.61 ± 0.13	1.06
4U 1954+319	41	0.17 ± 0.03	5.56 ± 1.04	1.35 ± 0.37	0.00 ± 1.23	1.07
4U 1954+319	54	0.06 ± 0.00	6.31 ± 0.33	6.00 ± 1.10	1.47 ± 0.06	1.04
4U 1954+319	55	0.09 ± 0.02	1.11 ± 0.34	1.62 ± 0.26	0.77 ± 0.07	1.09
4U 1954+319	74	0.13 ± 0.04	0.82 ± 0.54	0.97 ± 0.20	0.17 ± 0.22	1.06
4U 1954+319	75	0.07 ± 0.02	2.34 ± 0.82	1.20 ± 0.27	0.23 ± 0.21	1.01
4U 1954+319	Mean	0.14 ± 0.01	1.66 ± 0.30	0.99 ± 0.09	0.43 ± 0.18	1.79